PROCEEDINGS OF SPIE

Measuring in-vivo and in-situ ex-vivo the 3D deformation of the lamina cribrosa microstructure under elevated intraocular pressure

Junchao Wei, Bin Yang, Andrew P. Voorhees, Huong Tran, Bryn Brazile, et al.

Measuring in-vivo and in-situ ex-vivo the 3D deformation of the lamina cribrosa microstructure under elevated intraocular pressure

Junchao Wei [a], Bin Yang [a], Andrew P. Voorhees [a], Huong Tran [a, b], Bryn Brazile [a], Bo Wang [a, b], Joel Schuman [c], Matthew A. Smith [a, b], Gadi Wollstein [c], and Ian A. Sigal[*a, b]

[a] Department of Ophthalmology, University of Pittsburgh, Pittsburgh, PA, USA;
[b] Department of Bioengineering, University of Pittsburgh, Pittsburgh, PA, USA;
[c] NYU Langone Eye Center, NYU School of Medicine, New York, NY, USA.

* ian@OcularBiomechanics.com, Phone: 1 412-864-2220

ABSTRACT

Elevated intraocular pressure (IOP) deforms the lamina cribrosa (LC), a structure within the optic nerve head (ONH) in the back of the eye. Evidence suggests that these deformations trigger events that eventually cause irreversible blindness, and have therefore been studied in-vivo using optical coherence tomography (OCT), and ex-vivo using OCT and a diversity of techniques. To the best of our knowledge, there have been no in-situ ex-vivo studies of LC mechanics. Our goal was two-fold: to introduce a technique for measuring 3D LC deformations from OCT, and to determine whether deformations of the LC induced by elevated IOP differ between in-vivo and in-situ ex-vivo conditions. A healthy adult rhesus macaque monkey was anesthetized and IOP was controlled by inserting a 27-gauge needle into the anterior chamber of the eye. Spectral domain OCT was used to obtain volumetric scans of the ONH at normal and elevated IOPs. To improve the visibility of the LC microstructure the scans were first processed using a novel denoising technique. Zero-normalized cross-correlation was used to find paired corresponding locations between images. For each location pair, the components of the 3D strain tensor were determined using non-rigid image registration. A mild IOP elevation from 10 to 15mmHg caused LC effective strains as large as 3%, and about 50% larger in-vivo than in-situ ex-vivo. The deformations were highly heterogeneous, with substantial 3D components, suggesting that accurate measurement of LC microstructure deformation requires high-resolution volumes. This technique will help improve understanding of LC biomechanics and how IOP contributes to glaucoma.

Keywords: glaucoma, deformation, OCT, lamina cribrosa, image registration

1. INTRODUCTION

Glaucoma is the second leading cause of blindness in the world according to the World Health Organization (WHO)[1]. Although the mechanisms leading to glaucoma remain unclear, risk of the disease increases with elevated intraocular pressure (IOP), which is known to deform the lamina cribrosa (LC) in the optic nerve head (ONH)[1] (Figure 1a). The LC provides structural support to the retinal ganglion cell axons that transmit visual information to the brain as they exit the eye (Figure1b), and it is hypothesized that glaucomatous vision loss is the result of tissue damage within the ONH caused by excessive IOP-related LC deformation[2]. LC deformation has previously been studied with ex-vivo LC deformation testing[2-4], although these tests were conducted on enucleated eyes, and not in-situ. The development of optical coherence tomography (OCT) has spawned another set of studies of LC testing in-vivo[5,6]. However, it is not known how the deformation response of the LC differs between in-vivo and in-situ ex-vivo conditions, and which complicates obtaining a comprehensive understanding of LC mechanics. In this manuscript we present results from a study of how LC deformation induced by elevation of IOP differs between in-vivo and in-situ ex-vivo conditions. To do this, we present a new method to measure 3D LC deformation under elevated IOP from OCT images, which overcomes the challenges presented by speckle noise and shadowing artifacts. Specifically, as a proof-of-principle and to demonstrate the sensitivity of the technique, we focus on the deformations caused by a mild increase in IOP from 10 mmHg to 15 mmHg.

2. METHOD

2.1 Experiment

A healthy adult rhesus macaque monkey was used in the study. All procedures in this study were approved by the University of Pittsburgh's Institutional Animal Care and Use Committee (IACUC) and adhered to both the guidelines set forth in the National Institute of Health's Guide for the Care and Use of Laboratory Animals and the Association of Research in Vision and Ophthalmology (ARVO) statement for the use of animals in ophthalmic and vision research. The monkey was maintained on isoflurane anesthesia, and a 27-gauge needle was inserted into the anterior chamber of the eye and connected to a saline reservoir to control IOP via gravity perfusion (Figure 1c). IOP was initially set to 10 mmHg and gradually increased to 15 mmHg, 30 mmHg, and 40 mmHg (Figure 1d). During the in-vivo experiment, the intracranial pressure (ICP) was measured and controlled through cannulas in lateral ventricle and set at a fixed normal level 9 mmHg. At each IOP level, after allowing viscoelastic effects to dissipate, multiple OCT scans were taken by a spectral domain OCT (SDOCT), and the best quality scan was chosen for further computational analysis. The SDOCT has a higher speed and superior sensitivity than time domain OCT[7]. After the set of in-vivo scans were acquired, the monkey was sacrificed under deep anesthesia via exsanguination. Then, a set of in-situ ex-vivo scans were acquired following the same procedure for controlling IOP. Figure 1d illustrates the protocol for the experiment.
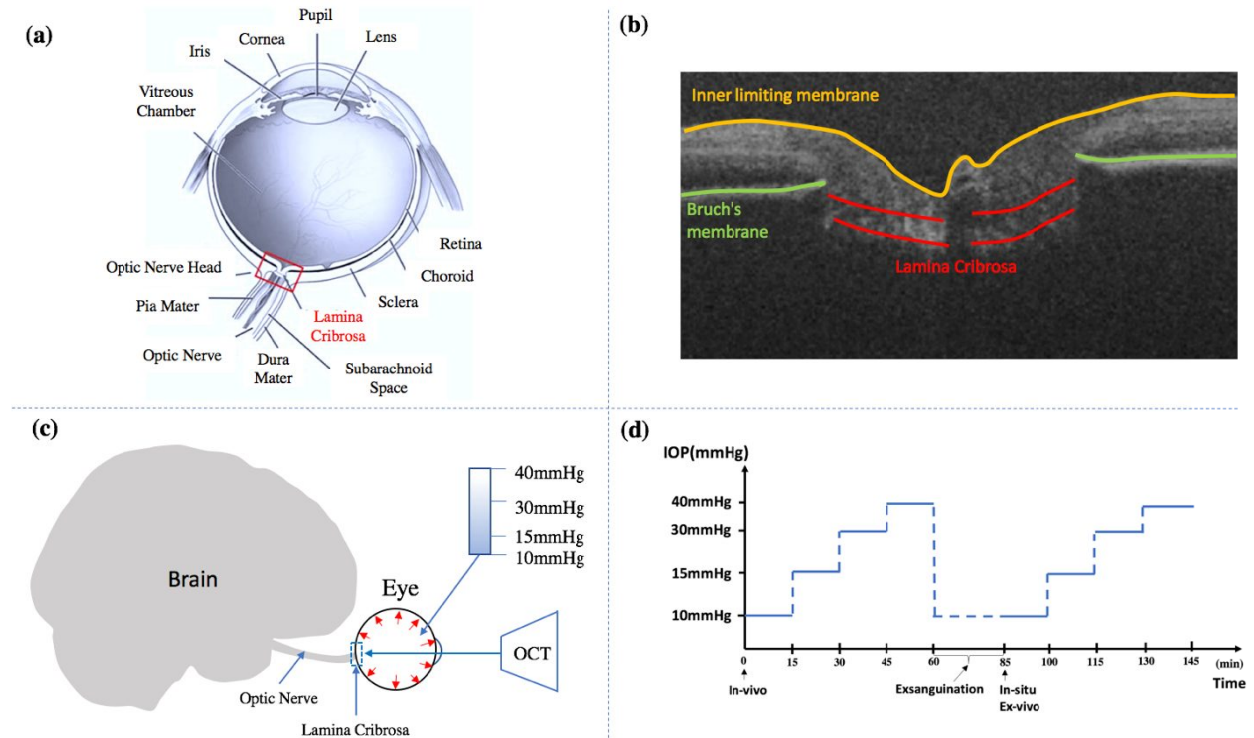
Figure 1 (a) Schematic longitudinal cross-section of the human eye, with the ONH highlighted with a red box. (b) An OCT B-scan shows the cross-section of the red box region in figure 1a, the lamina cribrosa is marked with double red lines, the yellow line shows the inner limiting membrane contacting with the vitreous humor, and the green line shows Bruch's membrane. In this in-vivo image a shadowing artifact through the middle of the lamina is apparent. (c) The brain and eye configuration for in-vivo and in-situ ex-vivo OCT scans, with IOP illustrated by red arrows. ICP can be transmitted to the eye through the optic nerve. (d) IOP was raised stepwise from 10mmHg to 40mmHg with each pressure step lasting about 15 minutes. While holding the pressure, the OCT scan was taken at each step of the in-vivo and in-situ ex-vivo experiments. Panel **a** modified[8], based on a diagram by the National Eye Institute. Panels **b** and **c** modified from[5].

2.2 Digital Volume Correlation

We used the Digital Volume Correlation (DVC)[9] technique to determine the deformation between multiple OCT scan images. For simplicity, the images were treated as 3D volumetric images. The basic concept of DVC is to establish a mapping between a reference image and a deformed image. The reference image was treated as a baseline image, which was then used to compare with each deformed image. The result of this mapping was a material transformation function between two volumes. Generally, we assume the following material transformation function:

$$\Phi(x) = x + U(x_0) \approx x + U(x_0) + F(x_0)(x - x_0) \tag{1}$$

$\Phi(x)$: Material Transformation at x
x_0: Reference Point Vector
x: Position Vector
$U(x_0)$: Grid Displacement Vector $[u, v, w]^T$
$F(x_0)$: Deformation Gradient Tensor at x_0: $F(x_0)_{ij}$

$$F(x_0)_{ij} = \begin{bmatrix} \frac{\partial u}{\partial x} & \frac{\partial u}{\partial y} & \frac{\partial u}{\partial z} \\ \frac{\partial v}{\partial x} & \frac{\partial v}{\partial y} & \frac{\partial v}{\partial z} \\ \frac{\partial w}{\partial x} & \frac{\partial w}{\partial y} & \frac{\partial w}{\partial z} \end{bmatrix} \tag{2}$$

The material transformation function will be evaluated through the minimization of the error of Zero-Normalized Cross Correlations (ZNCC)[10], which is a numerical metric for finding a similarity. There are many optimization methods to minimize the error of ZNCC. In the computation, we applied the Nelder-Mead method when the evaluation of gradients at direction of convergence is difficult[11].

$$e_{ZNCC} = 1 - \frac{\sum_{x \in D}(f(x) - \overline{f_D})(g(x') - \overline{g_{D'}})}{\sqrt{\sum_{x \in D}(f(x) - \overline{f_D})^2} \cdot \sqrt{\sum_{x' \in D'}(g(x') - \overline{g_{D'}})^2}} \tag{3}$$

D: Reference Image Subset
D′: Deformed Image Subset
f(x) : Voxel Value at x in Reference Image Subset
g(x′): Voxel Value at x′ in Deformed Image Subset
$\overline{f_D}$: Mean Value of Reference Image Subset
$\overline{g_{D'}}$: Mean Value of Deformed Image Subset

The minimization of correlation values indicates the best matching point in the search region of the deformed volume, and from the matched points the displacement vector can be calculated. The full-field deformation gradient can be computed from the displacement field at the matched points using a second order interpolation method[12]. The Lagrangian strain tensor (E) is then calculated as:

$$E = \frac{1}{2}(F^T F - I) \tag{4}$$

E: Lagrangian Strain Tensor
F: Deformation Gradient Tensor
I: Identity Tensor

From the strain tensor, the maximum shear strain and effective strain components were computed from the principal strains (eigenvalues of the strain tensor) using Eq. 5 and 6 respectively.

$$E_{max\,shear} = \frac{|P_1 - P_3|}{2} \tag{5}$$

P_1: First Principal Strain
P_3: Third Principal Strain

$$E_{effective} = \sqrt{\frac{2}{3}\varepsilon'_{ij}\varepsilon'_{ij}} \tag{6}$$

$\varepsilon'_{ij} = \varepsilon_{ij} - \overline{\varepsilon_{ij}}$: Deviatoric Strain
$\overline{\varepsilon_{ij}} = \frac{1}{3}\delta_{ij}\varepsilon_{kk}$: Hydrostatic Strain

The maximum shear strain is a measure of tearing and bending deformations; whereas, the effective strain is a singular measure of the total deformation including stretch and compression. Prior to analysis, OCT images were scaled to make the volumes isotropic, and the images were cropped to create a region of interest (ROI). A low pass filter and a 3D median filter were utilized to remove the speckle noise from OCT scan, and a sigmoid function was applied to improve the contrast of the image. To compute the deformations, we first aligned images globally using a linear transformation to reduce large rigid body motion and rotation, thus minimizing the pseudo-motions introduced into the experiment. Furthermore, it sped up the local search and optimization. The reversible linear transformation can be described using Eq. 7.

$$P_i' = C_T + R \cdot (P_i - C_s) \tag{7}$$

P_i' : New Voxel Point $[x_i \quad y_i \quad z_i]^T$

P_i : Old Voxel Point $[x_i' \quad y_i' \quad z_i']^T$

C_s : Rotation Center $[c_x \quad c_y \quad c_z]^T$

R : Rotation Tensor

To improve computational efficiency, we discretized the image domain numerically using seeds and nodes similar to a finite element mesh[13]. At each of those seeds, a material transformation was evaluated. Using those 'local' material transformations, the details of objects can be approximated and aligned. Since displacements at each node were different, this local alignment was nonlinear and could not be reversed. Once the computation was finished, we used the deformation vectors to check the registration. Several registration iterations were performed to make sure a good alignment of tissues until the change of Mean Square Error (MSE) between the reference image and the registered image is less than 1%. In addition, we verified the registrations by visual inspection throughout the volume.

3. RESULTS

Excellent registrations were obtained. In Figure 2, the in-vivo LC tissue registration verification is shown in the left-hand column and the in-situ ex-vivo LC tissue registration is shown in the right-hand column. The in-vivo LC has a significant blood vessel shadow region in the middle; whereas, the in-situ ex-vivo has remarkably little blood vessel shadow. The baseline pressure (10mmHg) image is shown in red while the elevated IOP image (15 mmHg) is shown in green, with yellow representing overlap. Before registration, the area of the unmatched region was large. After the registration, more yellow regions are noticeable, and the majority of the LC region was aligned well and the lamina pores were clearly visible. After registration, the correlation values, an indicator of image similarity, increased from 71.3% to 86.5% for in-vivo measurement and from 94.8% to 97.3% for in-situ ex-vivo scans. To make a fair comparison between in-vivo and in-situ ex-vivo conditions, the blood vessel shadow shown in the in-situ LC was manually selected and used as a mask on the in-situ ex-vivo LC (Figure 3). Figure 4 shows LC surfaces colored according to the strains measured between 10 mmHg and 15 mmHg for both in-vivo and in-situ ex-vivo conditions. In-vivo, the median effective strain at 15 mmHg, compared to baseline, was 1.5%, while the median effective strain in-situ ex-vivo was only 1%. Maximum strains reached levels above 3% in both conditions. From the variance of strain field, the in-vivo LC has a larger range of deformation when compared to the in-situ ex-vivo LC.

LC 3D Registration Comparison
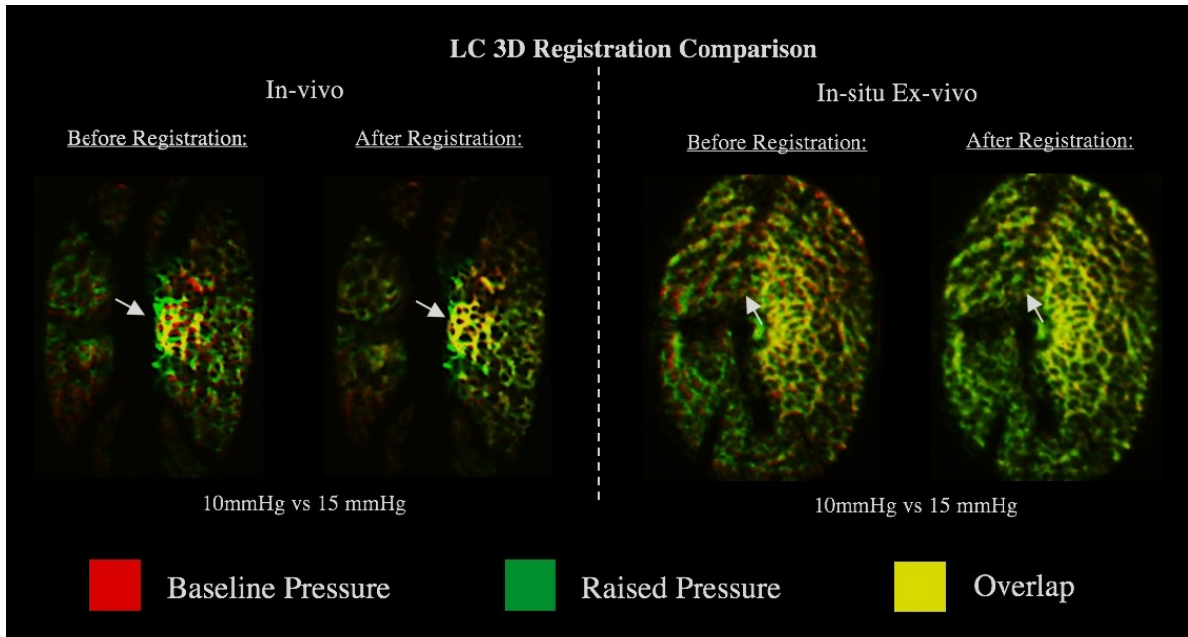
Figure 2 A good alignment of lamina cribrosa was achieved after 3D image registration between baseline pressure (red) and elevated pressure (green) for both in-vivo and in-situ ex-vivo measurements. Left column: in-vivo LC measurements show significant shadows at both pressures. After 3D registration, the overlapping region was increased (yellow); Right column: in-situ ex-vivo LC measurement show fewer shadows at both pressures. The overlapping region was also increased (yellow). The white arrows indicate a substantially improved overlap after registration.
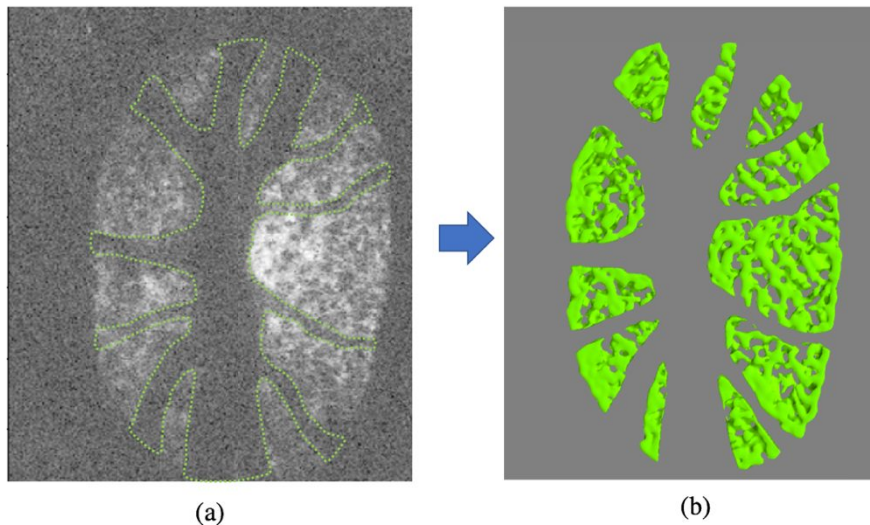
Figure 3 (a) Coronal (c-mode) section through the OCT volume of in-vivo LC measurement at baseline pressure. The outline of the vessel shadows was manually delineated and used to identify the region for comparison; (b) 3D LC surface from the in-situ ex-vivo scan masked using the outline from the in-vivo scan.
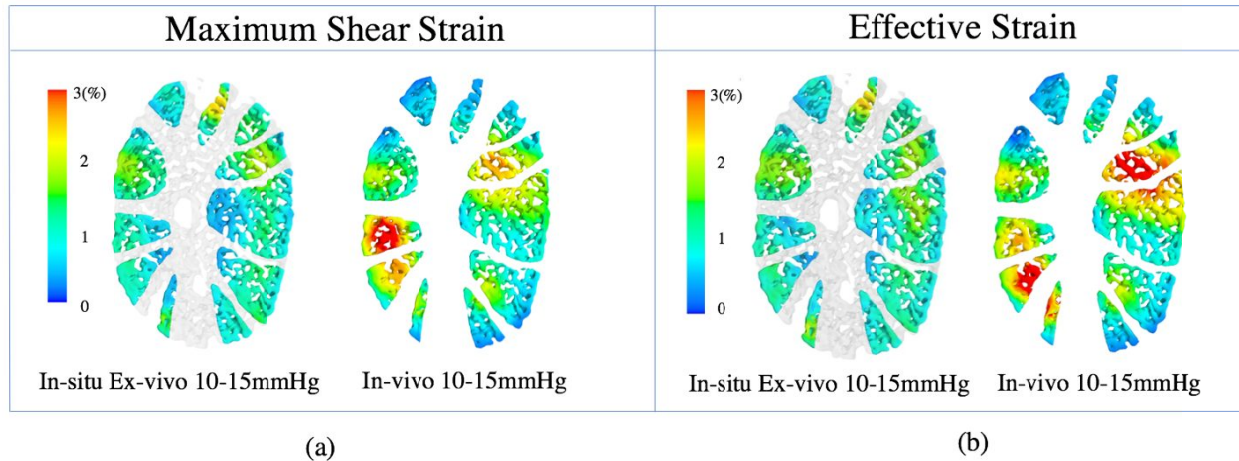
Figure 4 Strain deformations between baseline and elevated pressure were larger for in-vivo than for in-situ ex-vivo conditions, as shown here for (a) maximum shear strain and (b) effective strain.

4. DISCUSSION AND CONCLUSIONS

We developed a novel 3D OCT experimental and analysis technique to measure 3D LC deformations and demonstrated its feasibility for the measurement of IOP-induced LC deformations both in-vivo and in-situ ex-vivo conditions. We found that the LC deforms when IOP is raised, which is expected and in line with previous work[2,5,8]. Our novel experiments in-vivo and in-situ ex-vivo revealed that the in-vivo deformation of the LC was larger than the in-situ ex-vivo deformation measured for the same eye and the same pressure difference. The causes of the different LC mechanical behavior before and after death remain unclear. Nevertheless, it is important to quantitatively understand this difference to bridge the gaps between past and future in-vivo[14-16] and ex-vivo studies[17-19]. The ability to measure the in-vivo deformation of the LC is important, as it is hypothesized that large deformations of the LC contribute to glaucomatous damage and vision loss. In-vivo measurements of LC deformation could thus be used as a tool for the early detection, diagnosis, and tracking of glaucoma. Although we only present here the results for two pressure conditions, in future work, we will analyze the effects of other pressure changes. Our measurements are powerful because they focus on the effects in a single eye, imaged under identical conditions before and after death. Nonetheless, future work should also examine inter-individual variability in the response of the LC to elevated IOP, and on the differences between in-vivo and in-situ ex-vivo. Lastly, we will use this technique to analyze experimental data from human eyes to push these tools towards clinical translation.

4. ACKNOWLEDGEMENTS

REFERENCES

[1] Quigley, H. A. "Glaucoma: macrocosm to microcosm the Friedenwald lecture," Investigative ophthalmology & visual science. 46(8), 2663-2670 (2005).
[2] Sigal, I. A., Grimm, J. L., Jan, N. J., Reid, K., Minckler, D. S., & Brown, D. J. "Eye-Specific IOP-Induced Displacements and Deformations of Human Lamina Cribrosa," Investigative ophthalmology & visual science. 55(1), 1-15 (2014).

[3] Coudrillier, B., Geraldes, D. M., Vo, N., Albon, J., Abel, R. L., Campbell, I., & Ethier, C. R. "A novel micro-computed tomography (µCT) method to measure IOP-induced deformation of the Lamina Cribrosa (LC)," Investigative Ophthalmology & Visual Science. 56(7), 6149-6149 (2015).

[4] Midgett, D. E., Pease, M. E., Jefferys, J. L., Patel, M., Franck, C., Quigley, H. A., & Nguyen, T. D. "The pressure-induced deformation response of the human lamina cribrosa: analysis of regional variations," Acta biomaterialia. 53, 123-139 (2017).

[5] Tran, H., Grimm, J., Wang, B., Smith, M. A., Gogola, A., Nelson, S., ... & Sigal, I. A. "Mapping in-vivo optic nerve head strains caused by intraocular and intracranial pressures," Optical Elastography and Tissue Biomechanics IV International Society for Optics and Photonics. Vol. 10067, p. 100670B. (2017).

[6] Wang, B., Tran, H., Smith, M. A., Kostanyan, T., Schmitt, S. E., Bilonick, R. A., ... & Schuman, J. S. "In-vivo effects of intraocular and intracranial pressures on the lamina cribrosa microstructure," PloS one. 12(11), e0188302 (2017).

[7] Yaqoob, Z., Wu, J., & Yang, C. "Spectral domain optical coherence tomography: a better OCT imaging strategy," Biotechniques. 39(6) (2005).

[8] Sigal, I. A., Grimm, J. L., Schuman, J. S., Kagemann, L., Ishikawa, H., & Wollstein, G. "A method to estimate biomechanics and mechanical properties of optic nerve head tissues from parameters measurable using optical coherence tomography," IEEE transactions on medical imaging. 33(6), 1381-1389 (2014).

[9] Bay, B. K., Smith, T. S., Fyhrie, D. P., & Saad, M. "Digital volume correlation: three-dimensional strain mapping using X-ray tomography," Experimental mechanics. 39(3), 217-226 (1999).

[10] Lewis, J. P. "Fast template matching," In Vision interface, (Vol. 95, No. 120123, pp. 15-19) (1995).

[11] Wei, J. "In-situ Electronics Measurement Using X-ray Micro-Computed Tomography System and Data Driven Prognostic Health Management," Auburn University. (2017).

[12] Lall, P., & Wei, J. "X-ray micro-CT and digital-volume correlation based three-dimensional measurements of deformation and strain in operational electronics," In Electronic Components and Technology Conference (ECTC), IEEE 65th (pp. 406-416). IEEE (2015).

[13] Lall, P., & Wei, J. "X-ray micro-CT and DVC based analysis of strains in metallization of flexible electronics," In Thermal and Thermomechanical Phenomena in Electronic Systems (ITherm), 16th IEEE Intersociety Conference on (pp. 1253-1261). IEEE (2017).

[14] Zhang, L., Mani, B., Aung, T., Strouthidis, N. G., & Girard, M. J. "A fast method to measure the biomechanical properties of human optic nerve head tissues in vivo," Investigative Ophthalmology & Visual Science. 58(8), 3155-3155 (2017).

[15] Nadler, Z., Wang, B., Schuman, J. S., Ferguson, R. D., Patel, A., Hammer, D. X., ... & Wollstein, G. "In Vivo Three-Dimensional Characterization of the Healthy Human Lamina Cribrosa With Adaptive Optics Spectral-Domain Optical Coherence Tomography," Investigative ophthalmology & visual science. 55(10), 6459-6466 (2014).

[16] Wang, B., Nevins, J. E., Nadler, Z., Wollstein, G., Ishikawa, H., Bilonick, R. A., ... & Kraus, M. "Reproducibility of in-vivo OCT measured three-dimensional human lamina cribrosa microarchitecture," PLoS One. 9(4), e95526 (2014).

[17] Sigal, I. A., Flanagan, J. G., Tertinegg, I., & Ethier, C. R. "3D morphometry of the human optic nerve head," Experimental eye research. 90(1), 70-80 (2010).

[18] Nguyen, C., Midgett, D., Kimball, E. C., Steinhart, M. R., Nguyen, T. D., Pease, M. E., ... & Quigley, H. A. "Measuring Deformation in the Mouse Optic Nerve Head and Peripapillary Sclera," Investigative Ophthalmology & Visual Science. 58(2), 721-733 (2017).

[19] Perez, B. C., Pavlatos, E., Morris, H. J., Chen, H., Pan, X., Hart, R. T., & Liu, J. "Mapping 3D strains with ultrasound speckle tracking: method validation and initial results in porcine scleral inflation," Annals of biomedical engineering. 44(7), 2302-2312 (2016).